Inorganic Chemistry
Article
pubs.acs.org/IC

Geometrical Spin Frustration and Ferromagnetic Ordering in $(Mn_xPb_{2-x})Pb_2Sb_4Se_{10}$

Pierre F. P. Poudeu,* Honore Djieutedjeu, Kulugammana G. S. Ranmohotti, Julien P. A. M. Makongo, and Nathan Takas

Laboratory for Emerging Energy and Electronic Materials, Department of Materials Science and Engineering, University of Michigan, Ann Arbor, 48109, United States

Supporting Information

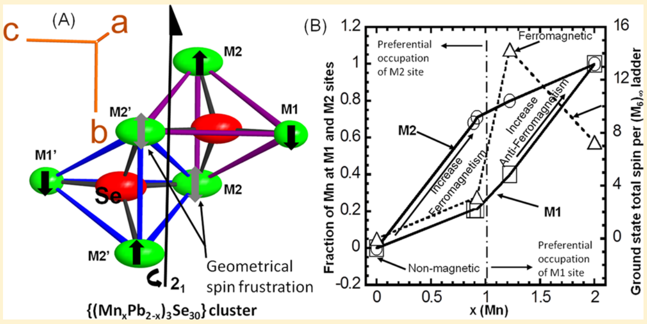

ABSTRACT: Engineering the atomic structure of an inorganic semiconductor to create isolated one-dimensional (1D) magnetic subunits that are embedded within the semiconducting crystal lattice can enable chemical and electronic manipulation of magnetic ordering within the magnetic domains, paving the way for (1) the investigation of new physical phenomena such as the interactions between electron transport and localized magnetic moments at the atomic scale and (2) the design and fabrication of geometrically frustrated magnetic materials featuring cooperative long-range ordering with large magnetic moments. We report the design, synthesis, crystal structure and magnetic behavior of $(Mn_xPb_{2-x})Pb_2Sb_4Se_{10}$, a family of three-dimensional manganese-bearing main-group metal selenides featuring quasi-isolated $[(Mn_xPb_{2-x})_3Se_{30}]_\infty$ hexanuclear magnetic ladders coherently embedded and uniformly distributed within a purely inorganic semiconducting framework, $[Pb_2Sb_4Se_{10}]$. Careful structural analysis of the magnetic subunit, $[(Mn_xPb_{2-x})_3Se_{30}]_\infty$ and the temperature dependent magnetic susceptibility of $(Mn_xPb_{2-x})Pb_2Sb_4Se_{10}$, indicate that the compounds are geometrically frustrated 1D ferromagnets. Interestingly, the degree of geometrical spin frustration (f) within the magnetic ladders and the strength of the intrachain antiferromagnetic (AFM) interactions strongly depend on the concentration (x value) and the distribution of the Mn atom within the magnetic substructure. The combination of strong intrachain AFM interactions and geometrical spin frustration in the $[(Mn_xPb_{2-x})_3Se_{30}]_\infty$ ladders results in a cooperative ferromagnetic order with exceptionally high magnetic moment at around 125 K. Magnetotransport study of the $Mn_2Pb_2Sb_4Se_{10}$ composition over the temperature range from 100 to 200 K revealed negative magnetoresistance (NMR) values and also suggested a strong contribution of magnetic polarons to the observed large effective magnetic moments.

■ INTRODUCTION

The prospect for information storage as the magnetization orientation of (1) individual single molecule magnets (SMMs) or (2) individual isolated ferromagnetic substructures (clusters, chains, etc.) embedded within a three-dimensional (3D) crystal structure, rather than an array of magnetic particles, holds great promise for the development of spin-based ultrahigh-density information storage devices for computing[1,2] and spintronic[3] applications. However, such spin-based devices require the design and fabrication of magnetic materials with high Curie transition temperatures (T_c) and the capability of maintaining stable intrinsic magnetization. This implies that the ideal magnetic compounds should combine high ground state total spin with a large easy-axis magnetic anisotropy.[4] Previous efforts have concentrated mainly on the design of organic ligand-based SMMs containing increasingly large polynuclear clusters, such as the Mn_{12} ($S = 10$),[5,6] and Mn_{19} ($S = 83/2$)[7] aggregates with the goal to achieve high ground state total spin and therefore a higher energy barrier to magnetization reversal (U). Unfortunately, this strategy to synthesize polynuclear clusters with large ground state total spins have not generated high T_c or high thermal barriers to spin inversion as anticipated from the mathematical equation $U = S^2|D|$ (where S is the total ground state and D is the easy-axis magnetoanisotropy parameter).[8] This is mainly due to the fact that large ground state total spin of polynuclear clusters are offset by low D values arising from the adverse interdependence of both the S and D parameters.[4,8,9] The weak magnetic anisotropy (low D values) in organic ligand-based SMMs presumably also arise from the zero-dimensional (0D) character of the mono(poly)-nuclear magnetic clusters and the flexibility of organic ligands, which makes it difficult to restrain the orientation of localized spins on magnetic atoms within the cluster. Furthermore, the large size of organic ligands and their poor electron delocalization inhibits intracluster exchange coupling, which is believed to mitigate the quantum tunneling relaxation process governing the loss of magnetization under zero applied field.[10] Therefore, new strategies to achieve stronger intracluster magnetic coupling in

Received: August 20, 2013
Published: December 17, 2013

dx.doi.org/10.1021/ic402128c | *Inorg. Chem.* 2014, 53, 209−220

low-nuclearity cluster SMMs are being explored to enhance their local magnetic moment, which could lead to a higher thermal barrier to spin inversion. For instance, it was recently shown that strong axial magnetic anisotropy can be achieved in SMMs by replacing organic ligands with less flexible polyoxometalates (POM) ligands.[11−22] In addition, it was also shown that the diffuse spin of a N_2^{3-} radical bridge in dinuclear lanthanide complexes led to exceptionally strong magnetic exchange interactions between the Ln atoms resulting in a large relaxation barrier.[23] However, the T_c's in these compounds remain quite low.

We proposed that designing purely inorganic geometrically frustrated semiconducting magnets containing one-dimensional (1D) magnetic subunits with strong intrachain antiferromagnetic exchange interactions between magnetic centers embedded within the inorganic semiconducting framework, may lead to high Curie transition temperatures and large magnetic moments (implying large *S*), which are necessary properties of promising magnetic materials for spin-based devices. Geometrically frustrated magnets are compounds in which the geometry of the magnetic sublattice constraints a large fraction of magnetic sites to randomly adopt several nearly degenerate spin configurations leading to disordered ground states. Classical examples are compounds containing two-dimensional (2D) geometrically frustrated magnetic lattices such as the Kagome lattice antiferromagnets, which consist of corner-sharing equilateral triangles[24−26] and triangular or hexagonal lattices formed by edge-sharing equilateral triangles[24,25] and compounds in which the magnetic lattice consists of a three-dimensional (3D) tetrahedron consisting of four edge-sharing equilateral triangles.[24,25]

One elegant approach to create 1D geometrically frustrated magnetic subunits embedded within a semiconducting matrix consists of crystal-engineering of the atomic structure of low symmetry binary and ternary semiconducting heavy main-group metal chalcogenides through atomic substitutions at targeted metal positions. We have successfully applied this approach to generate several ternary and quaternary ferromagnetic semiconductors containing isolated one-dimensional (1D) magnetic ladders uniformly distributed within a 3D semiconducting framework structure.[27−31] In this work, we focus our attention on the new family of quaternary compounds with general composition $(Mn_xPb_{2-x})Pb_2Sb_4Se_{10}$ $(0 \leq x \leq 2)$. This family of compounds was designed by isoelectronic substitutions of nonmagnetic Pb by magnetic Mn atoms at targeted atomic positions in the structure of $Pb_4Sb_4Se_{10}$.[32] Here we report the synthesis, crystal structure and magnetic properties of several compositions. We found that the crystal structure of $(Mn_xPb_{2-x})Pb_2Sb_4Se_{10}$ contains quasi-isolated 1D tetranuclear (M_4, for $x \leq 1$) or hexanuclear (M_6 for $x > 1$) magnetic ladders coherently embedded and uniformly distributed within a purely inorganic three-dimensional (3D) semiconducting framework. We attempt to correlate the observed magnetic behaviors to Mn content (*x* value), the geometry of the 1D magnetic sublattice and the degree of frustration within the magnetic sublattice. We show that the ability to manipulate the concentration and distribution of manganese atoms within the 1D magnetic ladder, $[(Mn_xPb_{2-x})_3Se_{30}]_\infty$, through isoelectronic substitution of the nonmagnetic Pb atoms by Mn atoms at the same metal positions, enables a simultaneous optimization of the degree of geometrical spin frustration and the strength of the intraladder AFM interactions. This maximizes the effective magnetic moment (total spin ground states) within individual isolated 1D $[(Mn_xPb_{2-x})_3Se_{30}]_\infty$ magnetic ladders.

■ RESULTS AND DISCUSSION

Synthesis and Characterization. Single phase products of the $(Mn_xPb_{2-x})Pb_2Sb_4Se_{10}$ (x = 1.0, 1.22 and 2.0) compounds were obtained from direct combination of the elements at high temperatures. Figure 1A shows X-ray diffraction patterns of the synthesized $(Mn_xPb_{2-x})Pb_2Sb_4Se_{10}$ (x = 1.0, 1.22) materials along with the theoretical pattern of $Mn_{1.22}Pb_{2.78}Sb_4Se_{10}$ (x = 1.22) simulated using single crystal structure data at 300 K. The excellent agreement between the theoretical pattern of $Mn_{1.22}Pb_{2.78}Sb_4Se_{10}$ and the experimental patterns of $(Mn_xPb_{2-x})Pb_2Sb_4Se_{10}$ (x = 1.0, 1.22) suggests the formation of isomorphic single phase products of both phases. The plot of the relative change in the lattice parameters with increasing Mn content is shown in Figure 1B. All three parameters (*a*, *b* and *c*) marginally decrease upon substituting Pb by Mn up to x = 1.0 and then contract sharply with further increases in Mn content ($1.0 \leq x \leq 2.0$). The calculated unit cell parameters of the full Mn composition (x = 2), assuming the retention of the orthorhombic space group *Pnma* (#62), are a = 24.09 Å, b = 4.04 Å, and c = 19.09 Å.

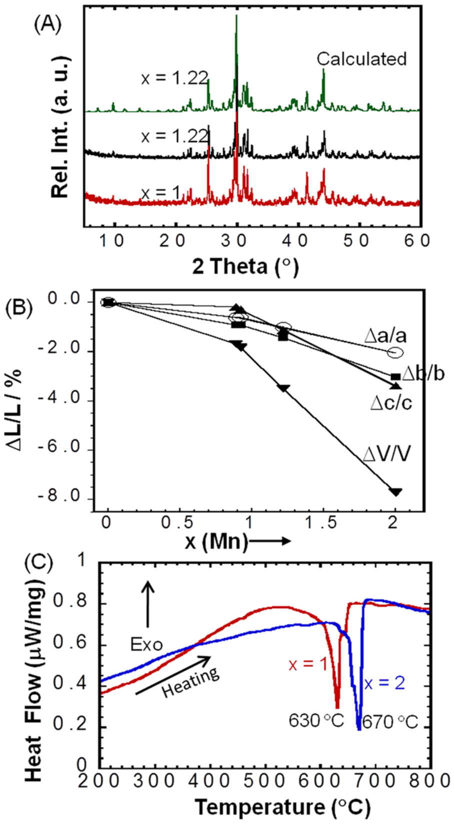

Figure 1. X-ray powder patterns, contraction in the unit cell parameters and differential scanning calorimetry (DSC) curves of (Mn_xPb_{2-x})-$Pb_2Sb_4Se_{10}$. (A) The Mn/Pb substituted compositions (x = 1.0, 1.22) show excellent agreement with the theoretical pattern calculated from the crystal structure of $Mn_{1.22}Pb_{2.78}Sb_4Se_{10}$. (B) Upon increasing the Mn content, a marginal reduction in the unit cell parameters is observed up to x = 1.0. Further increase in Mn content results in a sharp drop of the unit cell parameters. (C) Upon increasing the temperature, a single endothermic peak of melting with onset temperature of 630 °C (x = 1.0) and 670 °C (x = 2.0) was observed.

Table 1. Selected Crystallographic Data and Details of Structure Determinations for $Mn_xPb_{4-x}Sb_4Se_{10}$

formula sum	$Mn_{0.89}Pb_{3.11}Sb_4Se_{10}$ ($x = 0.89$) at 300 K	$Mn_{0.92}Pb_{3.08}Sb_4Se_{10}$ ($x = 0.92$) at 100 K	$Mn_{0.92}Pb_{3.08}Sb_4Se_{10}$ ($x = 0.92$) at 300 K	$Mn_{1.22}Pb_{2.78}Sb_4Se_{10}$ ($x = 1.22$) at 100 K	$Mn_{1.22}Pb_{2.78}Sb_4Se_{10}$ ($x = 1.22$) at 300 K
crystal system	orthorhombic	orthorhombic	orthorhombic	orthorhombic	orthorhombic
space group	*Pnma* (#62)	*Pnma* (#62)	*Pnma* (#62)	*Pnma* (#62)	*Pnma* (#62)
formula weight (g/mol)	1970.24	1967.67	1967.67	1920.38	1920.38
density (ρ_{cal}) (g/cm^3)	6.58	6.64	6.57	6.61	6.53
lattice parameters (Å)					
a =	24.442(5)	24.385(5)	24.441(2)	24.281(5)	24.341(5)
b =	4.129(1)	4.114(2)	4.128(1)	4.089(4)	4.107(1)
c =	19.721(4)	19.605(4)	19.698(2)	19.450(5)	19.535(4)
volume (Å^3); Z	1990(1); 4	1967(1); 4	1988(1); 4	1931(1); 4	1953(1); 4
crystal size (mm)	0.02 × 0.03 × 0.18	0.03 × 0.04 × 0.26	0.03 × 0.04 × 0.26	0.01 × 0.05 × 0.20	0.01 × 0.05 × 0.20
crystal shape, color	needle-shape, black	needle-shape, black		needle-shape, black	
diffractometer; radiation (Å)	IPDS 2T (Stoe); λ (Mo K_α) = 0.71073				
ω range; $\Delta\omega$°; $2\theta_{max}$	180; 0.8; 60.5°	180; 0.8; 58.3°	180; 0.8; 60.5°	180; 0.8; 58.1°	180; 1; 63.0°
index range	$-34 \le h \le 34, -5 \le k \le 5, -27 \le l \le 27$	$-33 \le h \le 33, -5 \le k \le 5, -26 \le l \le 26$	$-33 \le h \le 33, -5 \le k \le 6, -22 \le l \le 22$	$-31 \le h \le 31, -4 \le k \le 5, -25 \le l \le 25$	$-33 \le h \le 33, -5 \le k \le 6, -25 \le l \le 25$
measured reflections	45694	47853	45694	51585	60154
unique reflections	3304	2988	3300	2934	3640
R_{int}/R_σ	0.099/0.029	0.055/0.021	0.064/0.021	0.051/0.018	0.053/0.027
μ/cm^{-1}	504	507	502	493	487
No. of parameters	112	112	112	112	112
extinction correction x =	0.00005(1)	0.00006(2)	0.0001(1)	0.00009(2)	0.0005(1)
difference electron density (e/Å^3)	+1.18 to −1.04	+2.61 to −2.27	+1.29 to −1.14	+1.67 to −2.07	+1.84 to −2.42
R1($F_0 > 4\sigma(F_0)$)[a]	0.025	0.037	0.021	0.031	0.033
wR2 (all)[b]	0.062	0.11	0.051	0.072	0.065
GOF	1.183	1.811	1.248	1.333	1.313

[a] $R1 = \sum||F_0|-|F_c||/\sum|F_0|$ [b] $wR2 = [\sum w(F_0^2 - F_c^2)^2/\sum w(F_0^2)^2]^{1/2}$

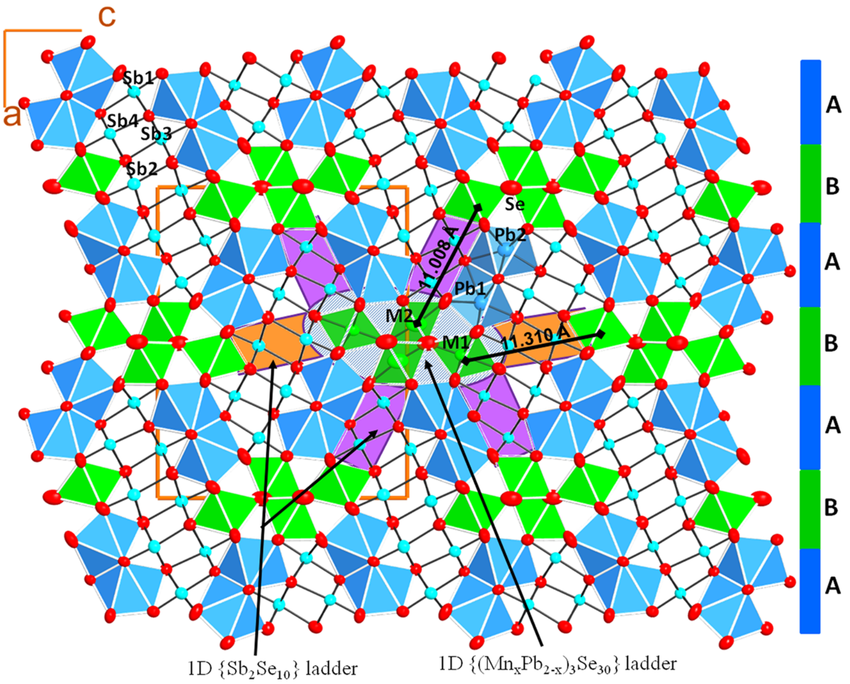

Figure 2. A representation of the 3D crystal structure of $(Mn_xPb_{2-x})Pb_2Sb_4Se_{10}$ projected along [010] and highlighting the quasi-isolated nearest neighboring 1D $[(Mn_xPb_{2-x})_3Se_{30}]_\infty$ magnetic ladders embedded within a 3D semiconducting $[Pb_2Sb_4Se_{10}]$ crystalline framework. The structure can also be regarded as "synthetic" superlattice of nonmagnetic layer A alternating along the *a*-axis with a magnetic layer B.

To further confirm the phase purity of the synthesized $(Mn_xPb_{2-x})Pb_2Sb_4Se_{10}$ (x = 1.0, 1.22 and 2.0) materials and to also determine their melting temperatures, differential scanning calorimetry (DSC) measurements were performed on finely ground powders. The endothermic onset temperatures are reported as the melting points (Figure 1C). The $(Mn_xPb_{2-x})Pb_2Sb_4Se_{10}$ (x = 1.0, 1.22 and 2.0) phases melt congruently between 630 °C for the composition with x = 1.0 and 670 °C for the composition with x = 2.0. The presence of a single endothermic peak of melting on the DSC curves supports the single phase nature of the synthesized materials. The observed increase in the melting temperatures with increasing Mn content is consistent with the large difference in the melting temperatures of MnSe (1535 °C) and PbSe (1078 °C).

Crystal Structure. Single crystal X-ray diffraction analysis of the structure of various compositions of the $(Mn_xPb_{2-x})Pb_2Sb_4Se_{10}$ solid-solutions revealed that despite the large contraction of the unit cell parameters (for x = 1.22: $\Delta a/a \sim 1.0\%$; $\Delta b/b \sim 1.2\%$; $\Delta c/c \sim 1.5\%$; $\Delta V/V \sim 3.5\%$) with increasing Mn content (Table 1) the compounds remain isostructural regardless of the Mn content (x value) crystallizing in the orthorhombic space group *Pnma* (#62) and adopting the $Fe_{0.75}Pb_{3.25}Sb_4Se_{10}$[27] (or $Pb_4Sb_4Se_{10}$[32]) structure-type. The observed large contraction of the unit cell parameters with increasing Mn content is consistent with the large difference ($\Delta R/R$ = 30%) in the effective ionic radii of Mn^{2+} (0.83 Å) and Pb^{2+} (1.19 Å) in a 6-fold coordination environment.[33,34] It is remarkable that despite the 30% difference in their ionic effective radii, a large fraction (more than 60%) of octahedrally coordinated Pb^{2+} in the structure of $Pb_4Sb_4Se_{10}$ can be substituted by Mn^{2+} without the collapse of the parent structure or any sign of symmetry reduction. This isomorphic substitution between Pb^{2+} and Mn^{2+} is in contradiction with the Goldschmidt atomic substitution rules,[35] which limit free substitution only between atoms with difference in effective ionic radii $\Delta R/R \leq 15\%$ and attests of the robustness of the structure of $Pb_4Sb_4Se_{10}$.

A polyhedral representation of the crystal structure of the $(Mn_xPb_{2-x})Pb_2Sb_4Se_{10}$ family of compounds is shown in Figure 2. The structure contains two crystallographically independent Pb atoms (Pb1 and Pb2), each located in an 8-fold coordinated position with bicapped trigonal prismatic geometry. Both bicapped trigonal prisms share faces and edges to form a double chain of paired bicapped trigonal prisms parallel to the b-axis. Four crystallographically independent Sb atoms (Sb1, Sb2, Sb3 and Sb4) are also found in 6-fold coordinated positions with distorted octahedral geometries. These octahedra around Sb atoms share edges and corners to form a two-octahedra thick and four-octahedra wide two-dimensional (2D) $[SbSe]_\infty$ ribbon with an Sb_2Se_3 structure type (Figure 2). In the crystal structure, four adjacent double-chains of paired bicapped trigonal prisms around Pb atoms are linked by $[SbSe]_\infty$ ribbons to build a three-dimensional (3D) structural framework containing large cylindrical voids. The cylindrical voids contain two crystallographically independent metal positions (M1 and M2), each located in a 6-fold coordination with distorted octahedral geometry. The M1 and M2 sites are the center of the isomorphic substitutions between Pb^{2+} and Mn^{2+} in the $(Mn_xPb_{2-x})Pb_2Sb_4Se_{10}$ solid-solutions. The octahedra around the M2 sites share edges to form a double $[M(2)_nSe_{5n}]_\infty$ ladder parallel to the b-axis, whereas octahedra around M1 sites share edges to form a one-dimensional $[M(1)_nSe_{4n+2}]_\infty$ single chain. The $[M(2)_nSe_{5n}]_\infty$ ladder is further linked to two adjacent $[M(1)_nSe_{4n+2}]_\infty$ single chains via corner-sharing to build the complex $[M(1)_nSe_{4n+2}]_\infty-[M(2)_nSe_{5n}]_\infty-[M(1)_nSe_{4n+2}]_\infty$ 1D magnetic sublattice with general composition $[(Mn_xPb_{2-x})_3Se_{30}]_\infty$. The structure of the $(Mn_xPb_{2-x})Pb_2Sb_4Se_{10}$ solid solutions can be divided into two important substructures. The first is the 1D $[(Mn_xPb_{2-x})_3Se_{30}]_\infty$ ladder of edges and corner-sharing octahedra of Se atoms containing the magnetic transition metal atom. This substructure will be thereafter referred to as the *magnetic subunit*. The second substructure is the 3D framework separating adjacent magnetic subunits and containing the nonmagnetic main group metals (Pb, Sb) and selenium atoms. This nonmagnetic substructure will be referred to as the *semiconducting subunit*. Alternatively, the structure of $(Mn_xPb_{2-x})Pb_2Sb_4Se_{10}$ can be regarded as a nanometer scale "synthetic" superlattice built up of ~0.7 nm thick magnetic (layer B) and nonmagnetic (layer A) layers parallel to the bc plane and alternating along the a-axis (Figure 2).

Crystal Chemistry of the Magnetic Subunit. The complex 1D magnetic subunit with general composition $[(Mn_xPb_{2-x})_3Se_{30}]_\infty$ is generated through a substitution of Pb atoms by Mn at distorted [2 + 4] octahedral positions in the structure of $Pb_4Sb_4Se_{10}$, and consists of four metal-centered (M1, M2, M1′ and M2′) octahedra sharing edges and corners within the ac plane and sharing edges along the b-axis to form a complex 1D $[(Mn_xPb_{2-x})_3Se_{30}]_\infty$ ladder (Figure 3A). Single crystal X-ray structure refinements (Table 2) of several compositions of the $(Mn_xPb_{2-x})Pb_2Sb_4Se_{10}$ ($0 \leq x \leq 2$) solid-solution series of isostructural phases and bond valence sum calculations,[36] suggested a 2+ oxidation state for the Mn atom and a preferential occupation of the M2 position (Figure 3D) for compositions

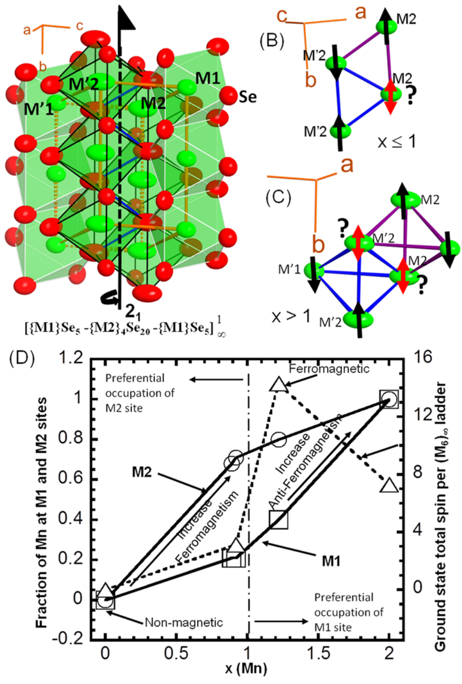

Figure 3. Structure and distribution of Mn within the $[(Mn_xPb_{2-x})_3Se_{30}]_\infty$ magnetic subunit. (A) A polyhedral representation of the 1D $[(Mn_xPb_{2-x})_3Se_{30}]_\infty$ substructure. Two examples of geometrically frustrated Mn lattices within the magnetic subunit: (B) edge-sharing nearly equilateral triangles ($x \leq 1$) and (C) edge-sharing tetrahedra ($x > 1$). (D) Preferential occupation of the M1 and M2 positions by Mn atoms within the 1D $[(Mn_xPb_{2-x})_3Se_{30}]_\infty$ ladder with increasing Mn content and the resulting ground state total spin, S_T. S_T is estimated from the fitting of high temperature inverse susceptibility data using the Curie–Weiss law. The fractions of Mn at the M1 and M2 positions reported on the graph were extracted from single crystal structure refinements of $(Mn_xPb_{2-x})Pb_2Sb_4Se_{10}$ with x = 0.89, 0.92 and 1.22 (Table 2).

Table 2. Site Occupancy Factors (k), Atomic Coordinates (Wyckoff Positions: $4c$), and Equivalent Isotropic Displacement Parameters U_{eq}/pm^2) for all atoms in the asymmetric unit of $Mn_xPb_{4-x}Sb_4Se_{10}$ (x = 0.89, 0.92 and 1.22) at 100 and 300 K[a]

atom	k	x	y	z	U_{eq}[b]	atom	k	x	y	z	U_{eq}[b]
Pb1	1	0.3728(2)	1/4	0.2979(2)	367(2)	Se1	1	0.2951(6)	3/4	0.3648(6)	259(4)
		0.3729(2)	1/4	0.2984(2)	151(6)			0.2939(3)	3/4	0.3644(3)	101(2)
		0.3723(1)	1/4	0.2977(1)	335(1)			0.2950(3)	3/4	0.3649(3)	218(2)
		0.3722(2)	1/4	0.2982(2)	208(5)			0.2951(2)	3/4	0.3644(3)	146(2)
		0.3719(1)	1/4	0.2973(1)	309(1)			0.2954(1)	3/4	0.3651(2)	175(1)
Pb2	1	0.2025(3)	1/4	0.3922(3)	361(2)	Se2	1	0.4187(5)	1/4	0.4407(5)	277(3)
		0.2026(2)	1/4	0.3930(2)	158(6)			0.4162(3)	1/4	0.4398(3)	159(2)
		0.2027(1)	1/4	0.3926(1)	334(1)			0.4180(3)	1/4	0.4401(3)	260(2)
		0.2015(2)	1/4	0.3958(2)	215(2)			0.4196(3)	1/4	0.4390(3)	227(2)
		0.2013(1)	1/4	0.3952(1)	303(1)			0.4201(2)	1/4	0.4393(2)	256(1)
Pb3	0.82(2)	0.5422(2)	1/4	0.2243(2)	318(3)	Se3	1	0.1352(4)	3/4	0.4810(5)	271(3)
	0.79(2)	0.5423(2)	1/4	0.2242(2)	107(1)			0.1347(3)	3/4	0.4803(3)	123(2)
	0.79(2)	0.5420(1)	1/4	0.2240(1)	249(2)			0.1349(3)	3/4	0.4807(3)	234(2)
	0.58(2)	0.5414(2)	1/4	0.2206(2)	182(2)			0.1344(2)	3/4	0.4819(3)	182(2)
	0.58(2)	0.5413(1)	1/4	0.2200(1)	236(1)			0.1346(1)	3/4	0.4823(2)	215(1)
Mn1	0.18(2)	0.5422(2)	1/4	0.2243(2)	318(3)	Se4	1	0.2686(5)	1/4	0.5324(6)	282(4)
	0.21(2)	0.5423(2)	1/4	0.2242(2)	107(1)			0.2677(3)	1/4	0.5320(3)	133(2)
	0.21(2)	0.5420(1)	1/4	0.2240(1)	249(2)			0.2686(3)	1/4	0.5325(3)	293(2)
	0.42(2)	0.5414(2)	1/4	0.2206(2)	182(2)			0.2690(2)	1/4	0.5325(3)	200(2)
	0.42(2)	0.5413(1)	1/4	0.2200(1)	236(1)			0.2699(1)	1/4	0.5330(2)	231(1)
Sb1	1	0.1932(3)	3/4	0.5945(4)	270(3)	Se5	1	0.2618(4)	3/4	0.7305(5)	256(3)
		0.1926(2)	3/4	0.5941(2)	120(2)			0.2616(2)	3/4	0.7305(3)	138(2)
		0.1931(1)	3/4	0.5943(2)	245(2)			0.2621(2)	3/4	0.7308(3)	233(2)
		0.1929(2)	3/4	0.5952(2)	189(2)			0.2629(2)	3/4	0.7323(3)	195(2)
		0.1932(1)	3/4	0.5950(1)	220(1)			0.2628(1)	3/4	0.7323(2)	230(1)
Sb2	1	0.5101(3)	3/4	0.4073(4)	185(2)	Se6	1	0.4631(4)	3/4	0.2838(5)	240(3)
		0.5103(2)	3/4	0.4082(2)	88(1)			0.4628(3)	3/4	0.2840(3)	124(2)
		0.5103(1)	3/4	0.4076(2)	168(1)			0.4631(3)	3/4	0.2836(3)	228(2)
		0.5103(2)	3/4	0.4054(2)	141(2)			0.4658(3)	3/4	0.2795(3)	257(2)
		0.5104(1)	3/4	0.4047(1)	189(1)			0.4657(1)	3/4	0.2791(2)	277(2)
Sb3	1	0.3424(3)	3/4	0.4845(4)	286(3)	Se7	1	0.6259(5)	3/4	0.1911(6)	312(4)
		0.3416(2)	3/4	0.4849(2)	149(1)			0.6252(3)	3/4	0.1913(3)	124(2)
		0.3422(1)	3/4	0.4848(2)	243(2)			0.6254(3)	3/4	0.1909(3)	258(2)
		0.3428(2)	3/4	0.4859(2)	174(2)			0.6211(3)	3/4	0.1909(3)	243(2)
		0.3435(1)	3/4	0.4860(1)	215(1)			0.6214(2)	3/4	0.1906(2)	265(2)
Sb4	1	0.3270(3)	1/4	0.6898(4)	196(2)	Se8	1	0.1342(5)	1/4	0.6536(5)	308(3)
		0.3265(2)	1/4	0.6892(2)	91(2)			0.1331(3)	1/4	0.6533(3)	182(2)
		0.3268(2)	1/4	0.6898(2)	207(2)			0.1335(3)	1/4	0.6536(3)	312(2)
		0.3278(2)	1/4	0.6907(2)	147(2)			0.1331(3)	1/4	0.6529(3)	272(2)
		0.3280(1)	1/4	0.6911(1)	182(1)			0.1332(2)	1/4	0.6532(2)	311(2)
Pb4	0.31(2)	0.0611(4)	1/4	0.5362(5)	362(5)	Se9	1	0.5847(5)	1/4	0.3715(6)	358(4)
	0.29(2)	0.0613(3)	1/4	0.5361(3)	173(2)			0.5845(3)	1/4	0.3725(3)	134(2)
	0.29(2)	0.0611(3)	1/4	0.5362(3)	318(3)			0.5849(3)	1/4	0.3719(3)	268(2)
	0.20(2)	0.0597(3)	1/4	0.5374(4)	339(3)			0.5841(2)	1/4	0.3688(3)	191(2)
	0.20(2)	0.0594(2)	1/4	0.5371(3)	390(3)			0.5848(1)	1/4	0.3683(3)	258(1)
Mn2	0.69(2)	0.0611(4)	1/4	0.5362(5)	362(5)	Se10	1	0.5017(6)	1/4	0.0831(6)	357(4)
	0.71(2)	0.0613(3)	1/4	0.5361(3)	173(2)			0.5012(3)	1/4	0.0826(3)	183(2)
	0.71(2)	0.0611(3)	1/4	0.5362(3)	318(3)			0.5011(4)	1/4	0.0828(3)	324(3)
	0.80(2)	0.0597(3)	1/4	0.5374(4)	339(3)			0.5019(3)	1/4	0.0830(4)	348(2)
	0.80(2)	0.0594(2)	1/4	0.5371(3)	390(3)			0.5023(2)	1/4	0.0829(3)	406(2)

[a] For each atomic site, the first, second, third, fourth and fifth lines refer to x = 0.89 (300 K), x = 0.92 (100 K), x = 0.92 (300 K), x = 1.22 (100 K) and x = 1.22 (300 K), respectively. [b] U_{eq} is defined as one-third of the trace of the orthogonalized U_{ij} tensor.

with low manganese contents ($0 \leq x \leq 1$), whereas an increasingly large fraction of Mn atoms is observed in the M1 position for Mn-rich phases ($1 \leq x \leq 2$). The structure of the resulting magnetic substructural unit may be better described by the spatial arrangement of metal atoms in the 1D $[(Mn_xPb_{2-x})_3Se_{30}]_\infty$ ladder (Figure 3B,C). The $[(Mn_xPb_{2-x})_3Se_{30}]_\infty$ ladder contains a 2-fold screw axis parallel to the b-axis and running through the middle of the Se−Se bond, which renders M1 and M2 equivalent by symmetry to M1′ and M2′, respectively. The structure of the magnetic subunit can therefore be described as consisting of (1) edge-sharing nearly equilateral triangles $[M_3]_\infty$ (Figure 3B, Table 3) formed by M2

Table 3. Geometric Parameters (Distances (Å), Angles (deg)) of the [Mn_3] Triangle and [Mn_4] Tetrahedron in the Structure of (Mn_xPb_{2-x})$Pb_2Sb_4Se_{10}$ (x = 0.0, 0.89, 0.92 and 1.22) at 300 K

geometric parameter	$x = 1.22$	$x = 0.92$	$x = 0.89$	$x = 0$[33]
M2—Se	2.697(5)	2.723(7)	2.735(2)	2.793
M2′—Se	2.725(9)	2.766(2)	2.765(2)	2.969
M1—Se	2.842(7)	2.955(8)	2.954(2)	2.970
M2—M2	4.107(2)	4.128(2)	4.129(2)	4.166
M2—M2′	3.831(2)	3.902(1)	3.901(2)	4.079
M2—M1	4.796(2)	4.923(2)	4.939(2)	5.043
M2′—M1	5.042(2)	5.146(2)	5.158(2)	5.317
M2—Se—M2	99.2(3)	98.6(3)	98.0(6)	96.4
M2—Se—M2′	89.9(2)	90.6(2)	90.4(4)	90.1
M2—Se—M1	119.9(2)	120.4(2)	120.5(3)	122.1
M2′—Se—M1	129.8(3)	128.2(3)	128.8(5)	127.1

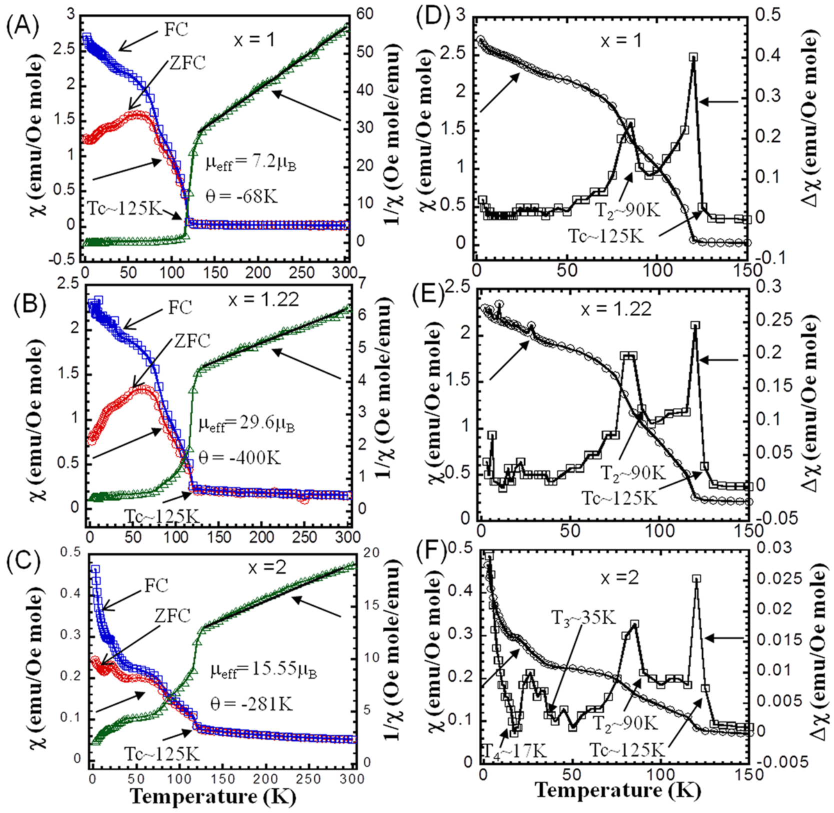

Figure 4. Temperature dependence of the DC magnetic susceptibility (χ), inverse susceptibility ($1/\chi$) and absolute change in the susceptibility ($\Delta\chi$) of various (Mn_xPb_{2-x})$Pb_2Sb_4Se_{10}$ compositions measured in an applied magnetic field of 100 Oe.

atoms (for Mn_xPb_{2-x})$Pb_2Sb_4Se_{10}$ compositions with $x \leq 1$) or (2) edge-sharing $[M_4]_\infty$ tetrahedra (for compositions with $x > 1$) linked by a 2-fold screw axis. The [M_4] tetrahedron consists of three crystallographically equivalent M2 atoms forming the nearly equilateral triangular base while the apical position is occupied by the M1 atom (Figure 3C, Table 3). Geometric details of the magnetic subunit indicate M----M interatomic distances ranging from 3.831(2) to 5.158(2) Å and M−Se−M bond angles ranging from 90.4° to 130° (Table 3). A strong antiferromagnetic (AFM) interaction is therefore anticipated between nearest neighboring Mn sites within the magnetic subunit. However, the triangular and tetrahedral geometry of magnetic subunits precludes AFM ordering on all Mn sites simultaneously (Figure 3B,C). This strongly points to the existence of geometrically frustrated magnetic interactions within individual 1D magnetic subunit in the structure of (Mn_xPb_{2-x})-$Pb_2Sb_4Se_{10}$ solid solutions.

Individual complex 1D $[(Mn_xPb_{2-x})_3Se_{30}]_\infty$ magnetic ladders in the 3D structure of (Mn_xPb_{2-x})$Pb_2Sb_4Se_{10}$ are surrounded by six neighboring similar magnetic ladders linked together by semiconducting 1D $[Sb_2Se_{10}]_\infty$ double chains of edge-sharing octahedra (Figure 2). The shortest interladder distances are: (1) M1·····M1 = 11.310(2) Å between $[(Mn_xPb_{2-x})_3Se_{30}]_\infty$ ladders within the same layer-B parallel to the *bc* plane and (2) M2·····M1 = 11.008(2) Å between ladders from adjacent layer B separated along the *a*-axis by a nonmagnetic layer A containing double chains of edge-sharing bicapped trigonal prismatic coordination around Pb atoms. This interladder distance of ∼11 Å leads to a surface density of $\sim 8 \times 10^{17}$ "magnetic subunits" per square meter. The large separation between magnetic subunits in the structure of (Mn_xPb_{2-x})$Pb_2Sb_4Se_{10}$ strongly points to weak magnetic exchange coupling between adjacent magnetic subunits (interladder interaction). Therefore, the magnetism of the $(Mn_xPb_{2-x})Pb_2Sb_4Se_{10}$ phases is dictated by the magnetic exchange coupling between nearest neighboring magnetic centers within individual magnetic subunit (intrachain interactions).

Magnetochemistry of the Magnetic Subunit. To probe the effect of the degree of Mn substitution (x values) and the distribution of Mn atoms within the 1D $[(Mn_xPb_{2-x})_3Se_{30}]_\infty$ magnetic subunits on the magnetic behavior of the $(Mn_xPb_{2-x})Pb_2Sb_4Se_{10}$ solid solutions, direct current (DC) magnetic susceptibility (χ_M) data on several compositions (x = 1.0, 1.22 and 2.0) were collected in the temperature range from 2 to 300 K. The temperature dependent molar susceptibility (χ) data under field cooled (FC) and zero-field cooled (ZFC), the inverse susceptibility ($1/\chi$) and the absolute variation in the susceptibility ($\Delta\chi$) for various samples are shown in Figures 4A−F. For the $(Mn_xPb_{2-x})Pb_2Sb_4Se_{10}$ sample with x = 1.0, the composition of the magnetic subunit is $[Mn_3Pb_3Se_{30}]_\infty$ and the distribution of Mn^{2+} atoms within the M1 and M2 positions are f_1 = 0.267(2) and f_2 = 0.733(2), respectively, where $x = f_1 + f_2$ (Figure 3D). If one neglects the contribution of Mn atoms in the M1 site, the magnetic behavior of this compound will be restricted to the interactions between nearest neighboring Mn atoms within the 1D $[Mn_3]_\infty$ ladder of edge-sharing equilateral triangles formed by the M2 atoms (Figure 3B). The magnetic susceptibility of this composition (x = 1) remains almost constant upon cooling to approximately 125 K and then sharply increases with further cooling below 125 K (Figure 4A). The rapid increase in the magnetic susceptibility is attributed to a ferromagnetic (FM) transition with a critical temperature T_c = 125 K. Fitting the high temperature inverse susceptibility data to the Curie−Weiss law (Figure 4A) yielded a negative θ_{CW} value (θ_{CW} = −68 K), suggesting an antiferromagnetic (AFM) exchange interaction between moments at neighboring Mn centers within the 1D $[Mn_3]_\infty$ magnetic ladder. However, the calculated effective magnetic moment, μ_{eff} = ~7.2 μ_B per Mn^{2+} ion, is larger than the value of 5.92 μ_B expected for Mn^{2+} ($3d^5$) in a spin-only approximation. This suggests the coexistence in the structure of FM and AFM magnetic exchange interactions between localized moments. The temperature dependent absolute change in the FC magnetic susceptibility (Figure 4D) shows two singularities at 125 and 90 K. The first peak at 125 K is attributed to the onset of the intraladder ($[Mn_3]_\infty$) ferromagnetic ordering, whereas the second peak is associated with the onset of a weak 3D antiferromagnetic long-range magnetic ordering between moments on neighboring magnetic units.

When the Mn content within the $[(Mn_xPb_{2-x})_3Se_{30}]$ magnetic unit is increased to x = 1.22, the new distribution of Mn atoms at M1 (f_1 = 0.42(2)) and M2 (f_2 = 0.80(2)) positions is obtained. Because both M1 and M2 sites contain a significant portion of Mn atoms, it is anticipated that the magnetic behavior of the resulting composition will be controlled by the interactions between Mn atoms within the 1D $[Mn_4]_\infty$ ladder of edge-sharing tetrahedra (Figure 3C). The temperature dependent FC and ZFC magnetic susceptibility data for x = 1.22 showed that the compound undergoes ferromagnetic ordering below 125 K, as revealed by the sharp increases in the susceptibility curves and the divergence of the FC and ZFC curves (Figure 4B). The down turn of the ZFC curve below 90 K and the presence of a second peak at 90 K on the temperature dependence of the $\Delta\chi$ curve (Figure 4E) suggest the onset of a 3D antiferromagnetic ordering similar to the one described above for the composition with x = 1.0. A large negative θ_{CW} value (θ_{CW} = −400 K) and a high μ_{eff} = ~29.6 μ_B per Mn^{2+} ion were derived from the fitting of the high temperature inverse susceptibility data using the Curie−Weiss law. The large negative θ_{CW} value indicates a very strong intrachain antiferromagnetic exchange interaction between moments on adjacent Mn centers whereas the calculated effective magnetic moments, which is 5 times larger than the expected spin-only μ_{eff} = 5.92 μ_B for Mn^{2+} ($3d^5$) suggests strong cooperative ferromagnetic coupling of residual moments arising from geometrical spin-frustration within individual magnetic units. The observed μ_{eff} = ~29.6.2 μ_B for the composition with x = 1.22 is equivalent to the effective magnetic moment anticipated for approximately 14.3 fully parallel spins. Therefore, the $[(Mn_xPb_{2-x})_3Se_{30}]$ magnetic unit in the composition with x = 1.22 can be regarded as a giant cluster of Mn atoms with total ground state spin of S_T = 14.3 (Figure 3D).

The magnetic subunit in the composition with x = 2 corresponds to a 1D $[Mn_6Se_{30}]_\infty$ hexanuclear magnetic cluster with full Mn occupancy at both M1 and M2 positions. The magnitude of the FC magnetic susceptibility of the resulting $Mn_2Pb_2Sb_4Se_{10}$ (x = 2) composition at 2 K is nearly 5 times smaller than that of the $Mn_{1.22}Pb_{2.78}Sb_4Se_{10}$ (x = 1.22) composition (Figure 4C). The temperature dependent FC and ZFC curves below the ferromagnetic ordering temperature, T_c = 125 K, are divergent with several broad peaks at 90, 35 and 17 K (Figure 4F), which can be associated with various competing FM and AFM interactions within the compound. A linear fit of the high temperature inverse susceptibility data using the Curie−Weiss law yielded a large negative θ_{CW} value (θ_{CW} = −281 K), indicating a very strong AFM coupling between Mn centers within the magnetic unit. The calculated effective magnetic moment μ_{eff} = ~15.55 μ_B per Mn^{2+} ion is 2.6 times larger than the value expected for spin only $Mn^{2+}(3d^5)$. This again suggests a cooperative ferromagnetic ordering of residual moments resulting from the geometrical spin frustration within the 1D $[Mn_6Se_{30}]_\infty$ hexanuclear magnetic unit in the structure of $Mn_2Pb_2Sb_4Se_{10}$. Therefore, the magnetic unit in the structure of $Mn_2Pb_2Sb_4Se_{10}$ can also be considered as a giant $[Mn_6]$ hexanuclear cluster of Mn atoms with total ground state spin of S_T = 7.3.

The observed ferromagnetic ordering in the $(Mn_xPb_{2-x})Pb_2Sb_4Se_{10}$ compounds suggested that the geometrical spin-frustration in the 1D $[(Mn_xPb_{2-x})_3Se_{30}]_\infty$ magnetic subunit of antiferromagnetically coupled Mn centers results in nonzero intrachain magnetic moments. A measure of the degree of geometrical spin-frustration is given by the parameter $f = |\theta_{CW}|/T_c$, where T_c is the cooperative ordering transition temperature and $f > 1$ indicates spin frustration.[24,37] Table 4 summarizes the effect of Mn substitution on the strength of the intrachain AFM exchange interactions, the degree of geometrical spin frustration and the magnitude of the effective magnetic moment on individual magnetic subunit in the corresponding compound. One can see from the values of θ_{CW}, f and μ_{eff} (Table 4) that the

Table 4. Effect of Mn Content on the Magnetic Interactions within the 1D $[(Mn_xPb_{2-x})_3Se_{30}]_\infty$ Magnetic Subunit[a]

x (Mn)	M1: f_1	M2: f_2	θ_{CW} (K)	T_c (K)	f	μ_{eff} (μ_B)	S_T
1.0	0.27	0.73	−68	125	0.54	7.2	3.13
1.22	0.42	0.80	−400	125	3.2	29.6	14.29
2.0	1.0	1.0	−281	125	2.3	15.5	7.28

[a] f_1 and f_2 are, respectively, the fraction of Mn at M1 and M2 sites.

strength of intrachain AFM coupling, the degree of spin frustration, as well as the magnitude of the effective magnetic moments in the magnetic subunit strongly, depend on both the concentration (x value) and distribution of Mn atoms at both M1 and M2 sites. Strong nearest-neighbor antiferromagnetic coupling is observed when a significant fraction of Mn atoms is present on both M1 and M2 sites with the strongest AFM exchange interaction observed for the composition with $x = 1.22$ ($\theta_{CW} = -400$ K) in which both atomic positions are partially occupied by a significant amount of Mn atoms. Likewise, spin frustration is only observed when both M1 and M2 sites contain a significant amount of Mn atoms with the strongest spin frustration corresponding to the composition with $x = 1.22$. It can be derived from the above discussion that the observed large effective magnetic moment is associated with the presence of a strong AFM nearest-neighbor exchange coupling and a mild spin-frustration within the magnetic subunit. Therefore, individual 1D $[(Mn_xPb_{2-x})_3Se_{30}]_\infty$ magnetic subunits in the structure of the $(Mn_xPb_{2-x})Pb_2Sb_4Se_{10}$ phases can be regarded as a giant cluster of Mn atoms with large ground state total spin, S_T (Figure 3D).

To probe the origin of the observed extraordinary large effective moments in $(Mn_xPb_{2-x})Pb_2Sb_4Se_{10}$ phases, we have performed temperature dependent resistivity measurements at zero applied fields as well as field dependent changes in the resistivity at various temperatures on the composition with $x = 2$ (Figure 5). Under zero applied magnetic fields, a positive thermopower value of ∼+600 μV/K and an electrical resistivity of 225 Ω·cm were measured at room temperature. The resistivity gradually increases with decreasing temperature, suggesting a p-type semiconducting behavior. The temperature dependence of the electrical resistivity was analyzed using the Arrhenius's law $\rho \sim \exp(Eg/2kT)$ (where k is the Boltzmann constant) and an electrical band gap Eg ∼ 0.495 eV was extracted from the fitting of the linear portion (200 K ≤ T ≤ 300 K) of the ln(ρ) versus $1/T$ curve (inset Figure 5A). However, a sharp change in the slope of the resistivity is observed at 200 K (Figure 5A). The resistivity increases nearly exponentially with further cooling, reaching at temperatures below 170 K, values too large (>60 kΩ·cm) to be accurately measured. The large electrical resistivity of the $Mn_2Pb_2Sb_4Se_{10}$ can be rationalized by considering the interactions between itinerant carriers (holes) and localized moments within the magnetic subunit. Delocalized carriers (holes), which act as magnetic glue among magnetic ions are also scattered by the localized spin on magnetic ions inducing high electrical resistance. In the absence of an external applied magnetic field, the weak short-range ferromagnetic ordering of residual intrachain moments as the sample is cooled to temperatures approaching the Curie transition temperature (T_c = 125 K) induces (1) localization of a fraction of itinerant carriers and/or (2) strong spin-scattering of itinerant carriers through magnetic exchange coupling. This results in the decrease of the carrier's density and mobility leading to the observed sharp rise of the electrical resistivity.

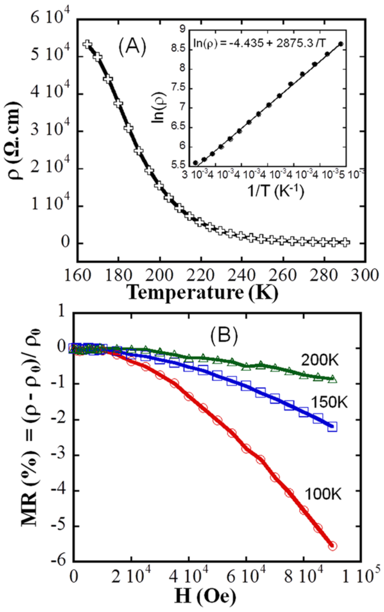

Figure 5. (A) Temperature dependent electrical resistivity of $Mn_2Pb_2Sb_4Se_{10}$ ($x = 2.0$) at zero applied magnetic fields. The inset indicates thermal activated conducting behavior between 200 and 300 K. (B) Field dependent change in the resistivity (MR = magnetoresistance) of $Mn_2Pb_2Sb_4Se_{10}$ at various temperatures.

Figure 5B shows the change in the electrical resistivity as a function of magnetic field (or magnetoresistance) for temperatures below and above the Curie transition temperature (T_c = 125 K). Negative magnetoresistance (NMR) values were observed from 100 to 200 K. This is attributed to decrease spin-scattering interactions between localized magnetic moments and itinerant carriers due to the relative alignment of residual intrachain localized magnetic moments upon application of an external applied field.[38−41] A sharper increase in the NMR values with rising applied magnetic field was observed at temperatures around the Curie transition. This suggests that around T_c, the parallel alignment of both the localized intrachain moments and the spin of conduction carriers along the direction of the external applied magnetic field minimizes spin-scattering of itinerant carriers by localized magnetic moments leading to an increase in their mobility. The observed NMR and the strong increase in its magnitude with increasing applied magnetic field strongly indicate the presence of spin-polarized itinerant carriers in the samples at temperatures around T_c. It was suggested that under the presence of an external applied field, the conducting-moments (spin-polarized itinerant carriers) can cluster into bound magnetic polarons (BMPs), that is, local short-range ferromagnetic ordering (FM) of polarized itinerate spins around the localized magnetic moments within the magnetic subunit.[41,42] The formation of such BMPs is believed to be responsible for the observed extraordinary large effective magnetic moments in $(Mn_xPb_{2-x})Pb_2Sb_4Se_{10}$ compositions. The final size of the BMPs and the magnitude of the magnetic moments originating from the interactions of neighboring BMPs are related to the fractions of (1) itinerant spin-polarized carriers and (2) localized spin-polarized carriers, which in turn depend on the Mn/Pb ratio within the magnetic subunit. This is due to the fact that the substitution of Pb^{2+} by Mn^{2+} reduces the ratio between itinerant spin-polarized carriers and localized spin-polarized carriers as well as increasing the concentration of magnetic centers. A large fraction of overlapping BMPs are expected when there is a good balance between the density of itinerant and localized spin-polarized carriers. This condition is best realized for the composition with $x = 1.22$ where there is a significant fraction of itinerant carriers from Pb atoms mixed with a significant fraction of localized carriers from Mn atoms leading to the observed large effective magnetic moment. For the composition with $x = 1$, the concentration of localized carriers is small, leading to the formation of a small fraction of BMPs. This is consistent with the observed small magnetic moment for this composition. Upon substituting all Pb atoms within the ladder by Mn atoms ($x = 2$), a large fraction of localized carriers is obtained. However, the fraction of itinerant carriers that would serve as glue between the localized carriers is negligible. This presumably results in small and nonoverlapping BMPs, which is consistent with the observed drop in the magnetic effective moment of the composition with $x = 2$, when compared to the sample with $x = 1.22$ (Figure 4C).

To confirm the ferromagnetic behavior of the $(Mn_xPb_{2-x})Pb_2Sb_4Se_{10}$ phases, field dependent magnetization measurements were performed at various temperatures above and below the magnetic ordering temperature of 125 K using polycrystalline powder samples with $x = 1.0$ and $x = 2.0$ (Figure 6). Above 125 K, the magnetization increases linearly with the applied magnetic field indicating paramagnetic behavior. Below 125 K, the magnetization rapidly increases upon a gradual increase of the applied field to 1000 Oe and exhibits linear field dependence thereafter. The hysteresis behavior of the magnetization curve with a coercive field on the order of 30 to 40 Oe confirms that the $(Mn_xPb_{2-x})Pb_2Sb_4Se_{10}$ phases are weak ferromagnets. However, the observed magnetization values are surprisingly low and the absence of magnetization saturation up to an applied field of 20 kOe (Figure 6A, inset) suggests that only a very small fraction of residual intrachain moments are aligned with respect to the applied magnetic field.

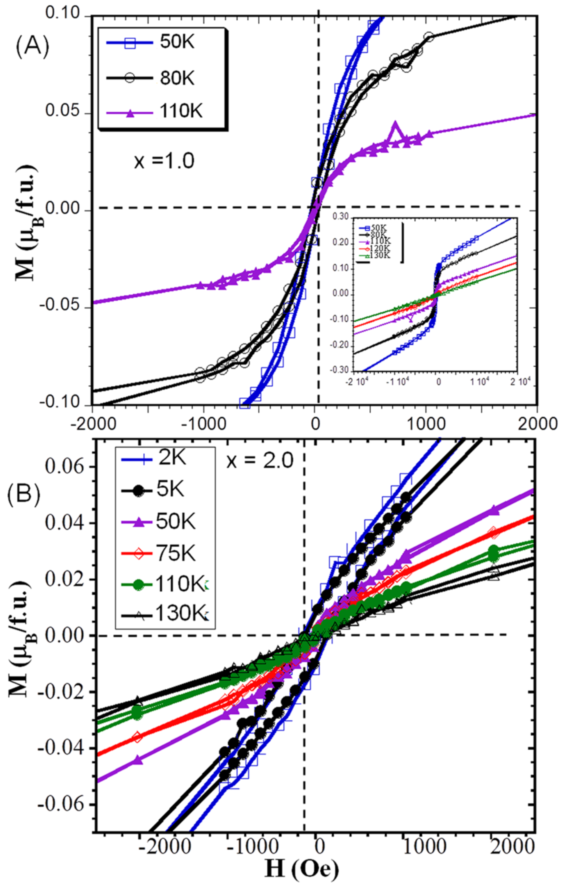

Figure 6. Field (H) and temperature (T) dependence of the magnetization (M) of $(Mn_xPb_{2-x})Pb_2Sb_4Se_{10}$ compositions ($x = 1.0$ and $x = 2.0$). Upon varying the magnetic field between +20 and −20 kOe, hysteresis behavior is observed at temperatures below 125 K, whereas a linear dependence of the magnetization with applied field is observed at higher temperatures (inset).

CONCLUSION

In summary, a new family of quaternary ferromagnetic semiconductors with general composition $(Mn_xPb_{2-x})Pb_2Sb_4Se_{10}$ was designed and the crystal structure and magnetic behavior of several compositions were investigated. The crystal structure of $(Mn_xPb_{2-x})Pb_2Sb_4Se_{10}$ contains complex magnetic 1D $[(Mn_xPb_{2-x})_3Se_{30}]_\infty$ magnetic subunits coherently embedded in a 3D semiconducting subunit of the main-group metal (Pb, Sb) and selenium atoms. We found that gradual Mn to Pb substitution within the magnetic unit maintains the crystal structure, leaving it essentially unchanged. However, the magnetic behavior of the resulting compound strongly depends on the concentration of Mn atoms (x value) and the distribution of Mn atoms at various metal positions within the magnetic subunit. All samples show ferromagnetic behavior with ordering temperature $T_c = 125$ K. However, fits of the high temperature inverse susceptibility data to the Curie−Weiss law yield negative θ_{CW} values, suggesting antiferromagnetic coupling between nearest neighbor magnetic centers within the 1D $[(Mn_xPb_{2-x})_3Se_{30}]_\infty$ magnetic subunit. The strength of the AFM coupling drastically increases when a significant amount of Mn atoms is present at both metal positions within the geometrically frustrating magnetic subunits. The strongest AFM coupling and the largest geometric spin frustration is observed for the composition with $x = 1.22$. This combination of strong intrachain nearest neighbor AFM coupling, a mild geometric spin frustration within the magnetic subunit, and the formation of BMPs is believed to be responsible for the existence of ferromagnetic ordering with large effective magnetic moments in the $(Mn_xPb_{2-x})Pb_2Sb_4Se_{10}$ solid solutions.

EXPERIMENTAL SECTION

Synthesis. Polycrystalline single phase powders of $(Mn_xPb_{2-x})Pb_2Sb_4Se_{10}$ ($x = 1.0$, 1.22 and 2) were synthesized by reacting mixtures of high purity elemental powders (Mn, 99.8%; Pb, 99.99%; Sb, 99.999%; Se, 99.999%) at a high temperature. The constituent elements weighed in the desired ratio (total mass =10 g) under an argon atmosphere in a dry glovebox were mixed in an agate mortar with a pestle and transferred into a fused silica tube ($\text{Ø}_{ID} = 9$ mm, length = 18 cm). The tube was flame-sealed under a residual pressure of ~10^{-3} Torr. The sealed tubes were placed into mullite tubes and were loaded into tube furnaces and heated to 800 K in 12 h and then dwelled for 96 h followed by cooling to room temperature in 12 h. Single crystals of $(Mn_xPb_{2-x})Pb_2Sb_4Se_{10}$ ($x = 1.0$ and 1.22) suitable for X-ray structure determination were grown by annealing the as-prepared polycrystalline single phase powders at 900 K for 7 days followed by cooling to room temperature in 24 h.

Characterization. *X-ray Powder Diffraction.* The phase purity of the synthesized $(Mn_xPb_{2-x})Pb_2Sb_4Se_{10}$ ($x = 1.0$, 1.22 and 2) polycrystalline samples were assessed by recording X-ray diffraction patterns on finely ground powders using Cu Kα radiation ($\lambda = 1.540\ 56$ Å) in reflection geometry on a PANalytical X-ray powder diffractometer with position sensitive detector and operating at 45 kV and 40 mA.

Differential Scanning Calorimetry (DSC). Differential scanning calorimetry (DSC) measurements were performed on finely ground powders of the synthesized $(Mn_xPb_{2-x})Pb_2Sb_4Se_{10}$ ($x = 1.0$, 1.22 and 2.0) materials to determine their melting temperatures and also to further confirm the phase purity. DSC data were recorded using approximately 10 mg of the synthesized materials and an equivalent mass of alumina (Al_2O_3) as the reference. Both the sample and the reference, sealed in a small quartz tube under residual pressure of 10^{-3} Torr, were placed on the sample and reference pans of a F401 DSC apparatus (NETZSCH) maintained under flowing nitrogen gas. The sample and reference were simultaneously heated to 1073 K at a rate of

Table 5. Selected Interatomic Distances (Å) in $Mn_xPb_{4-x}Sb_4Se_{10}$ (x = 0.89, 0.92 and 1.22)[a,b,c]

	x = 1.22 (100 K)	x = 1.22 (300 K)	x = 0.92 (100 K)	x = 0.92 (300 K)	x = 0.89 (300 K)	x = 0.0
Pb1—Se2	2.970(6)	3.010(5)	2.967(7)	3.018(8)	3.030(2)	2.988
Pb1—Se(1,1$^{\mathrm{i}}$)	3.057(5)	3.072(4)	3.019(5)	3.096(7)	3.100(2)	3.096
Pb1—Se6$^{\mathrm{i}}$	3.078(5)	3.091(4)	3.102(5)	3.044(5)	3.035(8)	3.101
Pb1—Se6	3.078(5)	3.092(4)	3.102(5)	3.044(5)	3.035(8)	3.101
Pb1—Se(8$^{\mathrm{ii}}$,8$^{\mathrm{iii}}$)	3.490(5)	3.487(4)	3.513(5)	3.514(5)	3.521(9)	3.513
Pb1—Se5$^{\mathrm{iii}}$	3.522(6)	3.515(5)	3.540(7)	3.539(7)	3.548(2)	3.557
Pb2—Se(3,3$^{\mathrm{i}}$)	3.105(5)	3.122(4)	3.082(5)	3.164(5)	3.168(9)	3.144
Pb2—Se(1,1$^{\mathrm{i}}$)	3.117(4)	3.132(3)	3.146(5)	3.106(6)	3.110(1)	3.109
Pb2—Se4	3.123(6)	3.168(5)	3.153(7)	3.192(8)	3.201(2)	3.163
Pb2—Se(7$^{\mathrm{iv}}$,7$^{\mathrm{v}}$)	3.293(5)	3.288(4)	3.245(6)	3.246(7)	3.235(2)	3.308
Pb2—Se5$^{\mathrm{iii}}$	3.295(6)	3.301(5)	3.303(7)	3.302(7)	3.306(2)	3.312
Pb3|Mn1—Se10	2.841(8)	2.842(7)	2.951(7)	2.955(8)	2.954(2)	2.970
Pb3|Mn1—Se(7,7$^{\mathrm{i}}$)	2.873(5)	2.888(4)	2.955(5)	2.972(6)	2.980(1)	2.976
Pb3|Mn1—Se(6, 6$^{\mathrm{i}}$)	2.978(5)	2.989(4)	3.060(5)	3.058(5)	3.061(8)	3.028
Pb3|Mn1—Se9	3.063(7)	3.083(6)	3.084(7)	3.096(8)	3.083(2)	3.018
Sb1—Se3	2.621(7)	2.623(5)	2.640(7)	2.653(7)	2.651(2)	2.691
Sb1—Se(8,8$^{\mathrm{vi}}$)	2.748(5)	2.765(4)	2.771(5)	2.783(5)	2.774(8)	2.839
Sb1—Se(4,4$^{\mathrm{vi}}$)	3.014(5)	3.028(4)	3.012(6)	3.024(6)	3.026(2)	3.012
Sb1—Se5	3.164(7)	3.172(5)	3.160(8)	3.173(8)	3.162(2)	3.119
Sb2—Se6	2.677(7)	2.684(6)	2.698(8)	2.701(8)	2.694(2)	2.710
Sb2—Se(9,9$^{\mathrm{vi}}$)	2.809(5)	2.828(4)	2.828(6)	2.842(7)	2.843(2)	2.883
Sb2—Se(2,2$^{\mathrm{vi}}$)	3.076(6)	3.084(4)	3.142(7)	3.125(6)	3.114(2)	3.129
Sb2—Se2$^{\mathrm{vii}}$	3.471(7)	3.487(5)	3.477(8)	3.474(9)	3.465(2)	3.509
Sb3—Se1	2.632(7)	2.637(5)	2.633(8)	2.629(8)	2.629(2)	2.675
Sb3—Se(4,4$^{\mathrm{vi}}$)	2.866(5)	2.874(4)	2.885(6)	2.894(6)	2.899(2)	2.910
Sb3—Se(2,2$^{\mathrm{vi}}$)	2.914(6)	2.921(4)	2.887(6)	2.909(6)	2.913(2)	2.924
Sb3—Se9$^{\mathrm{vii}}$	3.339(7)	3.339(5)	3.327(7)	3.338(8)	3.353(2)	3.321
Sb4—Se7$^{\mathrm{vii}}$	2.616(7)	2.619(5)	2.621(8)	2.625(8)	2.616(2)	2.656
Sb4—Se(5,5$^{\mathrm{i}}$)	2.706(5)	2.718(3)	2.719(5)	2.723(6)	2.730(9)	2.750
Sb4—Se(9$^{\mathrm{vii}}$,9$^{\mathrm{viii}}$)	3.178(5)	3.173(4)	3.225(6)	3.225(7)	3.221(2)	3.237
Sb4—Se4	3.391(7)	3.396(5)	3.400(8)	3.409(8)	3.417(2)	3.415
Mn2|Pb4—Se(10$^{\mathrm{ix}}$,10$^{\mathrm{x}}$)	2.684(7)	2.697(5)	2.719(6)	2.723(7)	2.735(2)	2.793
Mn2|Pb4—Se10$^{\mathrm{v}}$	2.731(9)	2.725(9)	2.752(9)	2.766(2)	2.765(2)	2.969
Mn2|Pb4—Se8	2.868(9)	2.895(8)	2.888(9)	2.91(1)	2.924(2)	2.892
Mn2|Pb4—Se(3,3$^{\mathrm{i}}$)	2.939(6)	2.952(5)	2.938(6)	2.951(6)	2.953(2)	3.028
Mn2|Pb4—Mn2|Pb4$^{\mathrm{xi}}$	3.834(9)	3.831(9)	3.897(9)	3.902(2)	3.902(2)	4.079

[a] Standard deviations corresponding to the last digits are indicated in brackets. [b] Corresponding bond distances in the $Pb_4Sb_4Se_{10}$ (x = 0)[32] parent structure are also included for comparison. [c] Operators for generating equivalent atoms: (i) $x, -1 + y, z$; (ii) $1/2 - x, -y, -1/2 + z$; (iii) $1/2 - x, 1 - y, -1/2 + z$; (iv) $-1/2 + x, -1 + y, 1/2 - z$; (v) $-1/2 + x, y, 1/2 - z$; (vi) $x, 1 + y, z$; (vii) $1 - x, 1 - y, 1 - z$; (viii) $1 - x, -y, 1 - z$; (ix) $1/2 - x, -y, 1/2 + z$; (x) $1/2 - x, 1 - y, 1/2 + z$; (xi) $-x, -y, 1 - z$; (xii) $1/2 - x, 2 - y, -1/2 + z$; (xiii) $1/2 - x, 2 - y, 1/2 + z$; (xiv) $1 - x, 2 - y, 1 - z$; (xv) $1/2 + x, 1 + y, 1/2 - z$; (xvi) $1/2 + x, y, 1/2 - z$.

20 K/min, isothermed for 2 min and then cooled to 473 K at a rate of 20 K/min. DSC data were recorded during two heating and cooling cycles.

Single Crystal Structure Determination. Single crystals of $(Mn_xPb_{2-x})Pb_2Sb_4Se_{10}$ phases with x = 0.89 (0.02 × 0.03 × 0.18 mm^3), x = 0.92 (0.03 × 0.04 × 0.26 mm^3) and x = 1.22 (0.01 × 0.05 × 0.20 mm^3) were mounted on the tip of a glass fiber using a two-component epoxy adhesive and intensity data were recorded at 300 K (x = 0.89, 0.92 and 1.22) and 100 K (x = 0.92 and 1.22) on a STOE IPDS-2T diffractometer using graphite-monochromated Mo Kα radiation (λ = 0.710 73 Å). Intensity data at all temperatures for all three crystals were indexed in the orthorhombic crystal system. The structure of $Mn_{0.89}Pb_{3.11}Sb_4Se_{10}$ (x = 0.89) at 300 K was refined in the orthorhombic space group *Pnma* (#62) by full-matrix least-squares techniques in the SHELTXL[43] package of programs using the atomic coordinates of $Fe_{0.75}Pb_{3.25}Sb_4Se_{10}$ as the starting model.[27] In the first refinement cycle, Pb atoms were located at the 8-fold position, M1(4*c*), with bicapped trigonal prismatic geometry and the 6-fold positions M2(4*c*), M3(4*c*) and M8(4*c*) with octahedral geometry. All Sb atoms were located at the 6-fold coordinated M4(4*c*), M5(4*c*), M6(4*c*) and M7(4*c*) octahedral positions. The refinement of this model yielded R_1 ~ 11% with reasonable thermal parameters for all atoms except Pb3 (M3) and Pb8 (M8), which showed slightly larger thermal parameters indicating mixed occupancies at both positions between Pb and a lighter element. In the second refinement cycle, Pb/Mn mixed site occupancy was considered at both M3 and M8 positions, resulting in more reasonable thermal parameters for all atoms with R_1 dropping below 5%. In the final refinement cycles, secondary extinction correction as well as anisotropic displacement parameters for all atoms were included. This resulted in the final atomic distribution M3 = 82%Pb/18%Mn, M8 = 31%Pb/69% Mn, corresponding to the final charge balanced composition $(Mn^{2+})_{0.89(2)}(Pb^{2+})_{3.11(2)}(Sb^{3+})_4(Se^{2-})_{10}$. The atomic positions of $Mn_{0.89}Pb_{3.11}Sb_4Se_{10}$ (x = 0.89) were used as the starting model for the refinement of the final distribution of Pb and Mn atoms at the M3 and M8 positions within the structures of $Mn_{0.92}Pb_{3.08}Sb_4Se_{10}$ (x = 0.92) and $Mn_{1.22}Pb_{2.78}Sb_4Se_{10}$ (x = 1.22) at 300 K. The Pb/Mn occupancy factor at both positions were freely refined to M3 = 79%Pb/21%Mn and M8 = 29%Pb/71%Mn, for $(Mn^{2+})_{0.92(2)}(Pb^{2+})_{3.08(2)}(Sb^{3+})_4(Se^{2-})_{10}$ and M3 = 58%Pb/42%Mn and M8 = 20%Pb/80%Mn, for $(Mn^{2+})_{1.22(2)}(Pb^{2+})_{2.78(2)}(Sb^{3+})_4(Se^{2-})_{10}$. A parallel refinement of the structures of $Mn_{0.92}Pb_{3.08}Sb_4Se_{10}$ (x = 0.92) and $Mn_{1.22}Pb_{2.78}Sb_4Se_{10}$ (x = 1.22) at 100 K revealed no major structural change and the distributions of Pb and Mn atoms at the M3 and M8 positions within the structures of $Mn_{0.92}Pb_{3.08}Sb_4Se_{10}$ (x = 0.92) and $Mn_{1.22}Pb_{2.78}Sb_4Se_{10}$ (x = 1.22) were similar to those obtained at 300 K. The observed distribution of Mn, Pb and Sb atoms at various metal positions as well as the assigned oxidation states Mn(2+), Pb(2+), Sb(3+), and Se (2−) are consistent with the results of bond valence sum (BVS) calculations[41] (M1(Pb), 2.1; M2(Pb), 2.0; M3(Pb/Mn), 2.3; M4(Sb), 2.5); M5(Sb), 2.6; M6(Sb), 2.7; M7(Sb), 2.9; M8(Mn/Pb), 1.5). The slight deviation of the calculated bond valence sum for Sb5, Sb6 and Sb7 atoms from the ideal value of 3.0 is attributed to the exceptionally long Sb−Se bond distances originating from the stereochemical activity of Sb electron lone-pair. Geometric parameters (distances (Å), angles (deg)) of the $[M_3]$ equilateral triangles and $[M_4]$ tetrahedron within the $[(Mn_xPb_{2-x})_3Se_{30}]_\infty$ ladder in the structure of $(Mn_xPb_{2-x})Pb_2Sb_4Se_{10}$ are gathered in Table 3. Summary of crystallographic data for $(Mn_xPb_{2-x})Pb_2Sb_4Se_{10}$ are given in Table 1. The atomic coordinates and isotropic displacement parameters of all atoms for $Mn_{0.89}Pb_{3.11}Sb_4Se_{10}$ (x = 0.89, at 300 K), $Mn_{0.92}Pb_{3.08}Sb_4Se_{10}$ (x = 0.92, at 100 and 300 K) and $Mn_{1.22}Pb_{2.78}Sb_4Se_{10}$ (x = 1.22, at 100 and 300 K) structures are given in Table 2. Selected interatomic distances are gathered in Table 5. The software, Diamond,[44] was utilized to create the graphical representation of the crystal structure with ellipsoid representations (98% probability level) for all atoms. Detailed crystallographic data can be obtained from the Fachinformationszentrum Karlsruhe, 76344 Eggenstein-Leopoldshafen, Germany (fax: +49−7247−808−666; E-mail: crysdata@fiz.karlsruhe.de) on quoting the depository number CSD- 424711 for $Mn_{0.89}Pb_{3.11}Sb_4Se_{10}$ (x = 0.89), CSD-425127 for $Mn_{0.92}Pb_{3.08}Sb_4Se_{10}$ (x = 0.92) at 100 K, CSD-424712 for $Mn_{0.92}Pb_{3.08}Sb_4Se_{10}$ (x = 0.92) at 300 K, CSD-425126 for $Mn_{1.22}Pb_{2.78}Sb_4Se_{10}$ (x = 1.22) at 100 K and CSD- 424713 for $Mn_{1.22}Pb_{2.78}Sb_4Se_{10}$ (x = 1.22) at 300 K.

Magnetic Property Measurements. Direct current (DC) temperature dependent magnetic susceptibility and isothermal field dependent magnetization measurements were performed on $(Mn_xPb_{2-x})Pb_2Sb_4Se_{10}$ (x = 1.0, 1.22 and 2.0) phases using a Quantum Design MPMS-XL SQUID magnetometer. The DC temperature dependent magnetic susceptibilities were investigated from 2 to 300 K under field cooled (FC) and zero-field cooled (ZFC) conditions. Approximately 50 mg of the as synthesized polycrystalline powder of $(Mn_xPb_{2-x})Pb_2Sb_4Se_{10}$ compounds was mounted inside a clear plastic straw sample holder, the magnetic moment contribution of which was subtracted from the combined (sample + sample holder) measurement. FC and ZFC magnetic susceptibility data were collected using an applied magnetic field of 100 Oe. Isothermal field dependent magnetization measurements were performed on randomly oriented polycrystalline grains of the $(Mn_xPb_{2-x})Pb_2Sb_4Se_{10}$ phases (x = 1.0 and x = 2.0) at various temperatures between 2 and 130 K, using external applied magnetic field ranging from −20kOe to +20 kOe.

Resistivity and magnetoresistance measurements. The zero-field cooled (ZFC) electrical resistivity data of $Mn_2Pb_2Sb_4Se_{10}$ was collected from 170 to 300 K on a $0.5 \times 1 \times 6$ mm^3 bar-shaped sample (cut from a hot pressed pellet) using the standard DC four-probe technique on a commercial Quantum Design Physical Property Measurement System (PPMS). The DC transverse magnetoresistance was measured in applied fields up to 85 kOe and at temperatures from 200 to 100 K.

■ ASSOCIATED CONTENT

Ⓢ Supporting Information

Crystallagraphic data in CIF format. This material is available free of charge via the Internet at http://pubs.acs.org.

■ AUTHOR INFORMATION

Corresponding Author

*P. F. P. Poudeu. Tel: +1-734-763-8436. Fax: +1-734-763-4788. E-mail: ppoudeup@umich.edu.

Notes

The authors declare no competing financial interest.

■ ACKNOWLEDGMENTS

This work was supported by the National Science Foundation (Career Award DMR-1237550).

Magnetic data were recorded on a SQUID magnetometer at the University of Michigan purchased using a MRI grant from the NSF (CHE-104008).

■ REFERENCES

(1) Leuenberger, M. N.; Loss, D. *Nature* **2001**, *410*, 789.

(2) Mannini, M.; Pineider, F.; Sainctavit, P.; Danieli, C.; Otero, E.; Sciancalepore, C.; Talarico, A. M.; Arrio, M. A.; Cornia, A.; Gatteschi, D.; Sessoli, R. *Nat. Mater.* **2009**, *8*, 194.

(3) Bogani, L.; Wernsdorfer, W. *Nat. Mater.* **2008**, *7*, 179.

(4) Neese, F.; Pantazis, D. A. *Faraday Discuss.* **2011**, *148*, 229.

(5) Sessoli, R.; Gatteschi, D.; Caneschi, A.; Novak, M. A. *Nature* **1993**, *365*, 141.

(6) Caneschi, A.; Gatteschi, D.; Sessoli, R.; Barra, A. L.; Brunel, L. C.; Guillot, M. *J. Am. Chem. Soc.* **1991**, *113*, 5873.

(7) Ako, A. M.; Hewitt, I. J.; Mereacre, V.; Clerac, R.; Wernsdorfer, W.; Anson, C. E.; Powell, A. K. *Angew. Chem., Int. Ed.* **2006**, *45*, 4926.

(8) Waldmann, O. *Inorg. Chem.* **2007**, *46*, 10035.

(9) Neese, F.; Solomon, E. I. *Inorg. Chem.* **1998**, *37*, 6568.

(10) Wernsdorfer, W.; Aliaga-Alcalde, N.; Hendrickson, D. N.; Christou, G. *Nature* **2002**, *416*, 406.

(11) AlDamen, M. A.; Cardona-Serra, S.; Clemente-Juan, J. M.; Coronado, E.; Gaita-Arino, A.; Marti-Gastaldo, C.; Luis, F.; Montero, O. *Inorg. Chem.* **2009**, *48*, 3467.

(12) AlDamen, M. A.; Clemente-Juan, J. M.; Coronado, E.; Marti-Gastaldo, C.; Gaita-Arino, A. *J. Am. Chem. Soc.* **2008**, *130*, 8874.

(13) Ibrahim, M.; Lan, Y. H.; Bassil, B. S.; Xiang, Y. X.; Suchopar, A.; Powell, A. K.; Kortz, U. *Angew. Chem., Int. Ed.* **2011**, *50*, 4708.

(14) Giusti, A.; Charron, G.; Mazerat, S.; Compain, J. D.; Mialane, P.; Dolbecq, A.; Riviere, E.; Wernsdorfer, W.; Bibouni, R. N.; Keita, B.; Nadjo, L.; Filoramo, A.; Bourgoin, J. P.; Mallah, T. *Angew. Chem., Int. Ed.* **2009**, *48*, 4949.

(15) Compain, J. D.; Mialane, P.; Dolbecq, A.; Mbomekalle, I. M.; Marrot, J.; Secheresse, F.; Riviere, E.; Rogez, G.; Wernsdorfer, W. *Angew. Chem., Int. Ed.* **2009**, *48*, 3077.

(16) Ritchie, C.; Ferguson, A.; Nojiri, H.; Miras, H. N.; Song, Y. F.; Long, D. L.; Burkholder, E.; Murrie, M.; Kogerler, P.; Brechin, E. K.; Cronin, L. *Angew. Chem., Int. Ed.* **2008**, *47*, 5609.

(17) Pichon, C.; Mialane, P.; Riviere, E.; Blain, G.; Dolbecq, A.; Marrot, J.; Secheresse, F.; Duboc, C. *Inorg. Chem.* **2007**, *46*, 7710.

(18) Dolbecq, A.; Dumas, E.; Mayer, C. R.; Mialane, P. *Chem. Rev.* **2010**, *110*, 6009.

(19) Proust, A.; Thouvenot, R.; Gouzerh, P. *Chem. Commun.* **2008**, 1837.

(20) Hill, C. L. *Chem. Rev.* **1998**, *98*, 1.

(21) *Polyoxometalates: from Platonic Solids to Anti-Retroviral Activity*; Pope, M. T., Mueller, A., Eds.; Kluwer Academic Publishers: Dordrecht, The Netherlands, 1994.

(22) Fang, X. K.; Kogerler, P.; Speldrich, M.; Schilder, H.; Luban, M. *Chem. Commun.* **2012**, *48*, 1218.

(23) Rinehart, J. D.; Fang, M.; Evans, W. J.; Long, J. R. *Nature Chem.* **2011**, *3*, 538.

(24) Ramirez, A. P. *Annu. Rev. Mater. Sci.* **1994**, *24*, 453.

(25) Greedan, J. E. *J. Mater. Chem.* **2001**, *11*, 37.

(26) Grohol, D.; Matan, K.; Cho, J. H.; Lee, S. H.; Lynn, J. W.; Nocera, D. G.; Lee, Y. S. *Nat. Mater.* **2005**, *4*, 323.

(27) Poudeu, P. F. P.; Takas, N.; Anglin, C.; Eastwood, J.; Rivera, A. *J. Am. Chem. Soc.* **2010**, *132*, 5751.

(28) Djieutedjeu, H.; Makongo, J. P. A.; Rotaru, A.; Palasyuk, A.; Takas, N. J.; Zhou, X. Y.; Ranmohotti, K. G. S.; Spinu, L.; Uher, C.; Poudeu, P. F. P. *Eur. J. Inorg. Chem.* **2011**, 3969.

(29) Ranmohotti, K. G. S.; Djieutedjeu, H.; Poudeu, P. F. P. *J. Am. Chem. Soc.* **2012**, *134*, 14033.

(30) Djieutedjeu, H.; Poudeu, P. F. P.; Takas, N. J.; Makongo, J. P. A.; Rotaru, A.; Ranmohotti, K. G. S.; Anglin, C. J.; Spinu, L.; Wiley, J. B. *Angew. Chem., Int. Ed.* **2010**, *49*, 9977.

(31) Poudeu, P. F. P.; Djieutedjeu, H.; Sahoo, P. *Z. Anorg. Allg. Chem.* **2012**, *638*, 2549.

(32) Skowron, A.; Brown, I. D. *Acta Crystallogr.* **1990**, *C46*, 2287.

(33) Shannon, R. D. *Acta Crystallogr., Sect. A: Cryst. Phys., Diffr., Theor. Gen. Crystallogr.* **1976**, *32*, 751.

(34) Shannon, R. D.; Prewitt, C. T. *Acta Crystallogr., Sect. B: Struct. Crystallogr. Cryst. Chem.* **1969**, *B 25*, 925.

(35) Goldschmidt, V. M. *J. Chem. Soc.* **1937**, 655.

(36) Brese, N. E.; Okeeffe, M. *Acta Crystallogr., Sect. B: Struct. Sci.* **1991**, 47, 192.

(37) Ramirez, A. P. *J. Appl. Phys.* **1991**, *70*, 5952.

(38) Toyozawa, Y. *J. Phys. Soc. Jpn.* **1962**, *17*, 986.

(39) Calderon, M. J.; Sarma, S. D. *Ann. Phys.* **2007**, *322*, 2618.

(40) Kaminski, A.; Das Sarma, S. *Phys. Rev. B* **2003**, *68*, 235210.

(41) Li, H. F.; Xiao, Y. G.; Schmitz, B.; Persson, J.; Schmidt, W.; Meuffels, P.; Roth, G.; Bruckel, T. *Sci. Rep.* **2012**, *2*, 1.

(42) Heikes, R. R.; Chen, C. W. *Physics* **1964**, *1*, 159.

(43) Sheldrick, G. M. *SHELTXL*; Bruker Analytical X-ray Instruments, Inc.: Madison, WI, 2000.

(44) Brandenburg, K. *Diamond*; Crystal Impact GbR: Bonn, Germany, 2005.